Chemical Engineering Journal 286 (2016) 610–621

Contents lists available at ScienceDirect

Chemical Engineering Journal

journal homepage: www.elsevier.com/locate/cej

The application of a novel fluidised photo reactor under UV–Visible and natural solar irradiation in the photocatalytic generation of hydrogen

Nathan Skillen [a], Morgan Adams [b], Cathy McCullagh [b], Su Young Ryu [c], Federica Fina [d], Michael R. Hoffmann [c], John T.S. Irvine [d], Peter K.J. Robertson [a,*]

[a] Centre for the Theory and Application of Catalysis (CenTACat), School of Chemistry and Chemical Engineering, Queen's University Belfast, David Keir Building, Stranmillis Road, Belfast BT9 5AG, UK
[b] Centre for Research in Energy and the Environment (CRE+E), School of Engineering, Robert Gordon University, The Sir Ian Wood Building, Garthdee Road, Aberdeen, AB10 7GJ, UK
[c] Linde-Robinson Laboratory, California Institute of Technology, Pasadena, CA 91125, United States
[d] JTSI Group, University of St. Andrews, School of Chemistry, Purdie Building, North Haugh, St Andrews KY16 9ST, UK

HIGHLIGHTS

- Photocatalytic reduction of water using Pt-C_3N_4 and $NaTaO_3$·La photocatalysts.
- Novel fluidised photoreactor for photocatalytic hydrogen evolution from water.
- Reactor parameters eliminated mass transfer limitations to increase photocatalytic activity.
- Water reduction achieved under both UV and direct solar irradiation.
- First use of solar telescope for irradiation of photocatalytic unit.

GRAPHICAL ABSTRACT

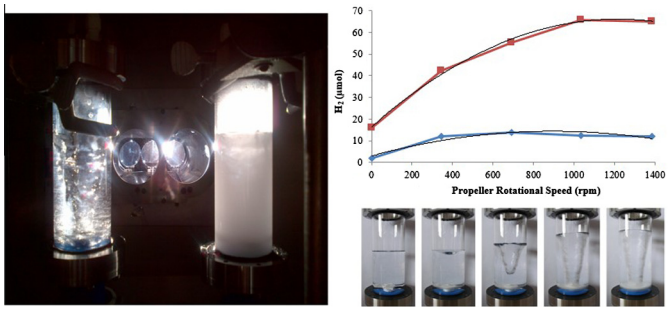

ARTICLE INFO

Article history:
Received 12 August 2015
Received in revised form 27 October 2015
Accepted 29 October 2015
Available online 4 November 2015

Keywords:
Hydrogen
Water splitting
Photocatalysis
Fluidised photo reactor
Solar light

ABSTRACT

With advancements in the development of visible light responsive catalysts for H_2 production frequently being reported, photocatalytic water splitting has become an attractive method as a potential 'solar fuel generator'. The development of novel photo reactors which can enhance the potential of such catalyst, however, is rarely reported. This is particularly important as many reactor configurations are mass transport limited, which in turn limits the efficiency of more effective photocatalysts in larger scale applications. This paper describes the performance of a novel fluidised photo reactor for the production of H_2 over two catalysts under UV–Visible light and natural solar illumination. Catalysts Pt-C_3N_4 and $NaTaO_3$·La were dispersed in the reactor and the rate of H_2 was determined by GC-TCD analysis of the gas headspace. The unit was an annular reactor constructed from stainless steel 316 and quartz glass with a propeller located in the base to control fluidisation of powder catalysts. Reactor properties such as propeller rotational speed were found to enhance the photo activity of the system through the elimination of mass transport limitations and increasing light penetration. The optimum conditions for H_2 evolution were found to be a propeller rotational speed of 1035 rpm and 144 W of UV–Visible irradiation, which produced a rate of 89 μmol h^{-1} g^{-1} over Pt-C_3N_4. Solar irradiation was provided by the George Ellery Hale Solar Telescope, located at the California Institute of Technology.

* Corresponding author. Tel.: +44 (0) 2890 974627.
E-mail address: p.robertson@qub.ac.uk (P.K.J. Robertson).

http://dx.doi.org/10.1016/j.cej.2015.10.101
1385-8947/

1. Introduction

Hydrocarbon based fuels (fossil fuels) are the primary resource for the worlds energy supplies. With increasing demand for global energy, however, there has been rapid growth in the field of energy development with a view towards the generation of an alternative energy source to provide global sustainability. Extensive focus is now being given to alternative sources such as wind, biomass, tidal, nuclear, solar, CO_2 recycling and H_2 production.

The photocatalytic reduction of CO_2 to products such as CH_3OH and CH_4 [1–4] is a viable approach for CO_2 recycling, however is yet to be implemented on a large scale. An alternative to this is the photocatalytic splitting of water for the generation of H_2. This is an attractive proposal as it utilises two abundant resources; H_2O and solar illumination. The splitting of pure H_2O into H_2 and O_2, shown in Eq. (1), is described as an 'uphill reaction' where a large positive change in the Gibbs free energy is observed ($\Delta G_o = -238$ kJ mol^{-1}) [5]. To achieve H_2O splitting the conductance band of the catalyst must be more negative than the reduction potential of H^+ to H_2 (0 V vs NHE at pH 0), Eq. (2). The valence band must also be more positive than the oxidation potential of H_2O to O_2 (1.23 V vs NHE at pH 0) [5], Eq. (3).

$$2H_2O \rightarrow 2H_2 + O_2 \quad (1)$$

$$2H^+ + 2e^- \rightarrow H_2 \quad (2)$$

$$2H_2O + 4h^+ \rightarrow O_2 + 4H^+ \quad (3)$$

Research into photocatalytic water splitting technology has become abundant with emphasis on both catalyst and system design [5–7]. Systematically the concept of clean energy driven large scale photocatalytic H_2O splitting is reliant on two factors; the efficient delivery of natural photons and the transfer of target species to photocatalyst surfaces.

Despite the simplistic concept of photocatalytic driven H_2 production, there are limited publications that investigate reactor engineering for increased H_2 production. A number of more recent publications have focused on pure water splitting in which a two-compartment or 'H-shaped' reactor is used in conjunction with a membrane to yield separate production streams of H_2 and O_2 [8–14]. This approach generally adopts a Z-scheme process which utilises two photocatalysts to overcome the stringent requirements faced by a single catalyst [9,14,15].

The single catalyst approach typically utilises a one-compartment reactor and will focus on increasing hydrogen production through maximising mass transfer and light distribution [16]. In view of this there are a number of advantages in developing a fluidised photocatalytic system including; improved mass transfer, excellent irradiation distribution and a high photocatalysts surface area-to-volume ratio [17–21]. Fluidisation is achieved as a result of the gravitational force of the catalyst particles becoming equal to the aerodynamic drag. Traditional methods of fluidisation utilise an upward stream of gas or fluid [17–19,21], however, previous examples have reported the use of external fields such as sound- and magnetic-assisted based fluidisation methods [20,22,23]. Examples of fluidised photocatalytic reactors have been reported using a range of model compounds including toluene [17], trichloroethylene [19], formaldehyde [20], NOx [18] and oxalic acid [21]. There are a limited number of fluidised based systems presented in the literature for water splitting or water reduction, however, in 2012 Reilly and colleagues [16] reported the construction of a UV-irradiated fluidised bed for H_2 production. The design concept of the reactor employed a low power internal illumination source (50 W) in a recirculating annular style fluidised system, which produced an optimum H_2 rate of 198 μmol h^{-1} over Pt loaded TiO_2.

At the critical point of fluidisation, the light penetration of a system can be increased as the dense particle bed becomes suspended and shows fluidic characteristics. In an attempt to utilise light efficiently, previous studies have used internal illumination sources [16,17] 'light guiding' particles [17] and optical fibres [19] that can direct light deeper into the catalyst bed. Kuo and colleagues found that the addition of SiO_2 particles to their system increased light scattering and thus, toluene removal. In this investigation, a propeller-stirred fluidised system is adopted which creates cavitation of the liquid reaction medium and thus maximises light penetration.

Irradiation characteristics must be carefully considered in any photocatalytic system, particularly in a fluidised system to ensure a more efficient method for future scale up. Moreover, if photocatalytic production of H_2 is to be utilised as an alternative fuel the development of photocatalytic reactors must also focus towards systems which are capable of utilising solar radiation. A common approach used in a number of the systems reported, however, involves high power lamps, which are positioned above a reactor to provide illumination through a quartz window typically with an area of ~15 cm^2 [24–26]. These systems utilise medium and high power lamps with a range of 300–450 W [24,27–30]. These lamps have been used in conjunction with novel catalysts to produce a range of yields of H_2 production. In 2012, Liu and Syu [24] reported a production rate of 14.9 μmol g^{-1} h^{-1} of H_2 under irradiation from a 450 W xenon lamp. Increased rates of H_2 have been shown by Khan and Qureshi [27] and Jeong et al. [28]. Khan and Qureshi produced H_2 at a rate of 180 μmol/h over $BaZr_{0.96}Ta_{0.04}O_3$ under irradiation from a 300 W xenon lamp. While there are numerous examples of systems that use high power lamps in the visible region, examples of reactors being deployed for H_2 production under natural irradiation are limited. Previous publications have used compound parabolic concentrators (CPC) based units to generate H_2 from H_2O, activated sludge and H_2S [31–35]. The system presented here utilises low power artificial irradiation sources that are easily scalable in an array structure. An alternative approach to CPC designs was adopted by utilising a solar telescope to concentrate natural illumination.

This paper reports the development of a novel fluidised photo reactor suitable for use with UV–Visible and natural solar illumination. The performance of the reactor has been evaluated through monitoring the evolution of H_2 over two photo catalysts, Pt-C_3N_4 and $NaTaO_3$·La. H_2 production using sustainable sources is a desirable approach in achieving clean driven fuel production. The application of low powered (36 W) visible lamps were examined with a view towards incorporation into large scale array structures. The feasibility of solar driven photocatalysis for H_2 production was demonstrated using the George Ellery Hale Telescope. This investigation aimed to demonstrate that photo reactor properties can significantly enhance the activity of a photo catalytic system, which can aid the applicability of photocatalytic technology for industrial applications.

2. Experimental

2.1. Materials

Catalysts graphitic carbon nitride (denoted as g-C_3N_4 hereafter), platinised carbon nitride (denoted as Pt-C_3N_4) and lanthanum doped $NaTaO_3$ (denoted as $NaTaO_3$·La hereafter) were all synthesised by collaboration partners for this study. The full details of the catalyst development along with the methodology can be found in the following publications [36–39].

2.2. Catalyst characterisation

Catalyst g-C_3N_4 was synthesized via solid state synthesis by thermal condensation of melamine at 550 °C in air. Loading of the platinum co-catalyst (Pt-C_3N_4) was performed by impregnation and subsequent calcination at 180 °C. g-C_3N_4 was suspended in an aqueous solution of hexachloroplatinic acid hexahydrate (1 g/L) and the solvent was evaporated at 80 °C. The resulting powder was then calcined at 180 °C for 2 h.

$NaTaO_3$:La was prepared by a conventional solid-state reaction. The starting materials, La_2O_3 (Strem Chemicals; 99.9%), Na_2CO_3 (J.T. Baker), and Ta_2O_5 (Strem Chemicals; 99.8%), were mixed in the ratio Na:La:Ta = 1 − X:X:1 supposing that the sodium ions were replaced by lanthanum ions. The excess amount of sodium (5 mol%) was added in the mixture to compensate the volatilization. The mixture was calcined in air at 1170 K for 1 h and 1420 K for 10 h with intermediate grinding. The excess sodium was washed out with water after calcination. After filtration, the powder was dried at 320 K in air. The crystal structures of synthesized NaTaO:La sample was confirmed by powder X-ray diffraction (XRD) using a Philips diffractometer (X'pert Pro) with Cu-Kα radiation. Diffuse reflectance spectrum was obtained with a UV–Vis spectrometer (Shimadzu SoildSpec-3700) and was converted from reflection to absorption spectra by the Kubelka–Munk method. X-ray Photoelectron Spectroscopy (XPS) was used to observe the changes in the oxidation states of Ta and O with doping of La with Al-Kα radiation.

2.3. Reactor development

The Propeller Fluidised Photo Reactor (denoted as PFPR hereafter) was capable of providing a controllable air tight environment in which photocatalysts could be agitated to facilitate desired photocatalytic transformations in gas, solid, liquid and vapour phases. The PFPR was an annular reactor constructed from 316 stainless steel (SS) and quartz glass and consisted of a quartz glass body with SS flange and caps with a motor embedded into the base, Fig. 1. The SS flange was designed to have the quartz embedded in engineering grade, high temp resistant silicone sealant. Into this flange piece a Viton O-ring (Barnwell) groove was machined, the combination of these produced a water and gas tight seal.

The reactor environment was controlled through two Swagelok needle bonnet valves and a custom built needle extraction valve, (Fig. 1). The custom port was constructed from a Swagelok SS 316 nipple fitting consisting of a Viton O-ring (Barnwell) and GC grade septa (Hewett-Packard). This port was utilised for gas headspace needle extraction sampling. The reactor seals were tested for leaks with a Thermo Scientific GC Leak Detector. The silicone sealant also provided a failsafe had the reactor vessel become pressurised, as it will rupture before the quartz.

The unit had a calculated capacity of ~210 mL with an operating capacity of 100 mL allowing a 110 mL gas headspace volume. The minimum and maximum operating capacities were 60 mL and 180 mL respectively giving a 150 mL and 30 mL gas headspace volume.

Fluidisation in the PFPR was achieved through the rotation of a 38 mm 4 blade SS 316 propeller located at the base of the reactor, Fig. 2. The propeller was driven by a 12 dcV motor, typically operating in the range 0–8 dcV by a bench top power supply. This optimum range allowed the propeller to rotate at speeds of 0–1730 rpm. This range of rotational speed gave a high level of control over both the mixing capabilities of the propeller and upward thrust required to bring stationary particles to a fluidised state in gas, vapour and liquid phases.

2.4. Illumination sources

2.4.1. Artificial illumination sources

The primary source of illumination for the PFPR was an illumination box consisting of commercially available low power 36 W lamps which emitted light in the UV and visible spectrum, Fig. 3. The mirrored Perspex box was designed to house four 36 W compact non-integrated fluorescent lamps along with nine air flow control fans. The PFPR was positioned centrally in the illumination box unit to allow for full irradiation exposure.

The spectral output of the lamps is shown in Fig. 4. The lamps provided an UV emission peak at 365 nm, where the remaining strong emissions in the visible region were 435, 436, 489, 546, 588 and 611 nm.

2.4.2. Solar illumination

Solar illumination was provided by The George Ellery Hale Solar Telescope, positioned on the roof of the Linde and Robinson building at California Institute of Technology (CalTech), Pasadena. The telescope, which is capable of continuously monitoring and tracking the sun, was operated during the period of 24th July to the 14th August 2012. Light was delivered through a series of angled mirrors and illumination shafts. The power density, temperature and humidity of the telescope were monitored with a pyranometer. During the period of operation the mean power density was in the range of 800–900 W m^2, the temperature ranged from 22.9 to 23.6 °C and the humidity from 978 to 981 hPa. Fig. 5(a) shows the position of the telescope on the Linde and Robinson building while Fig. 5(b), shows the mirrors contained within the structure which guide light down an illumination shaft to lower levels in the building. Fig. 5(c) shows a series of 3 mirrors which are located part way down the primary illumination shaft and guide the stream of solar light through a secondary illumination shaft and out through a series of quartz windows. Fig. 5(d) shows light exciting the second illumination shaft and irradiating two PFPR units.

2.5. Photocatalytic procedure

H_2 production was performed in the PFPR over catalysts Pt-C_3N_4 and $NaTaO_3$·La. In a typical experiment, a 1 g L^{-1} loading weight of catalyst was dispersed in 100 mL of aqueous medium containing 0.025 M oxalic acid and Milli-Q water. The PFPR was purged with Ar gas for 30 min to eliminate the presence of air in the system, during which time the rotation of the propeller was 289 rpm. After purging, the rotation of the propeller was increased to the desired level and illumination commenced. The unit was exposed to 6 h of illumination with gas head space samples taken at designated intervals.

Sample analysis was performed by gas chromatography at the University of St. Andrews and CalTech. The system used at the University of St. Andrews was an Agilent 3000 Micro GC with a dual gas carrier system (Ar and He) equipped with a TCD and molecular sieve column (HP 5890 Series II). The system used at the California Institute of Technology was a HP GC equipped with a TCD and molecular sieve (HP 5890 Series II) with N_2 as a carrier gas. Sample analysis at the University of St. Andrews was achieved by directly drawing a sample from the outlet of the PFPR via the GC internal pump. Analysis at CalTech was conducted by extraction from the injection port of the PFPR by SGE needles and directly injected into the CalTech HP GC.

The Formal Quantum Efficiency (FQE) of H_2 production in the PFPR was calculated as the reaction rate divided by the total light intensity of the UV–Visible lamps (Eq. (4)) [40]. The total light intensity irradiating the reactor surface was determined to be

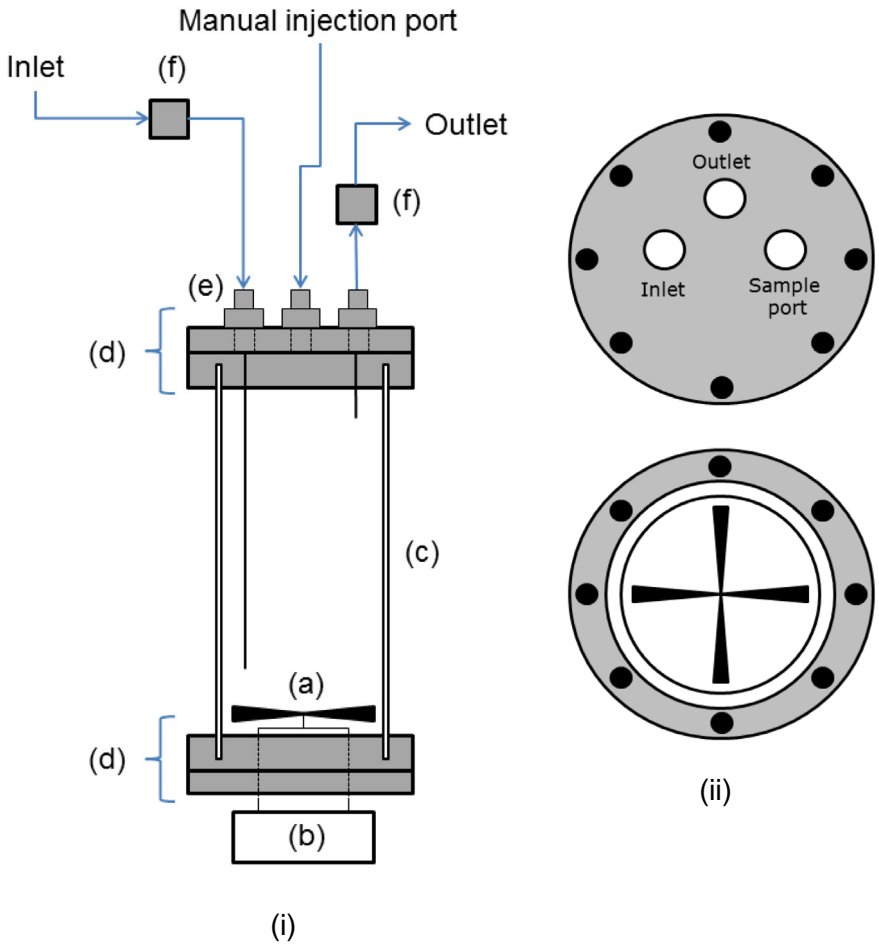

Fig. 1. (i) (a) Gas inlet, outlet valves and sample port, (b) cap and flange, (c) quartz chamber, (d) propeller and (e) motor and flange, (ii) top – cap and port arrangement, bottom – propeller.

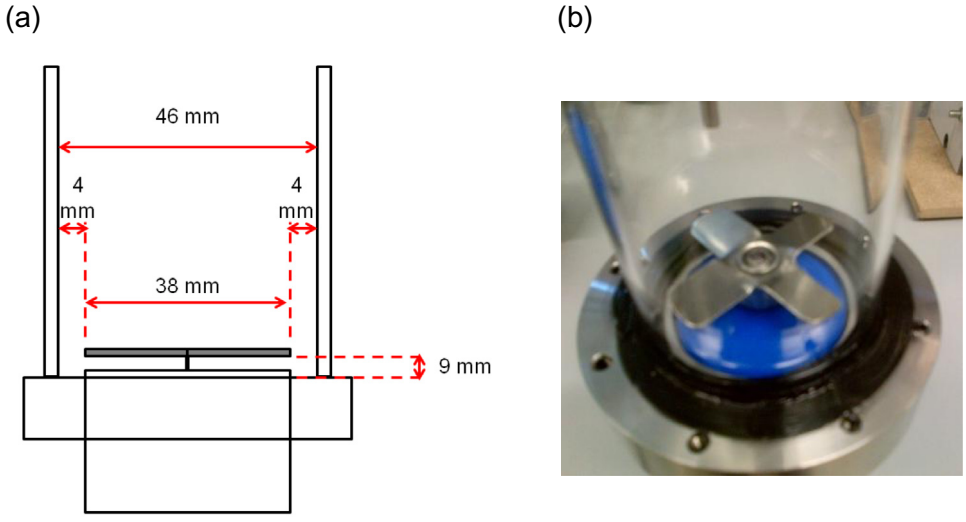

Fig. 2. (a) Cross section schematic of propeller positioning in the PFPR Model II and (b) image of 4 blade SS propeller.

396 μE cm^{-2} h^{-1} using a Lutron LX101 light meter (Lutron Electronic Enterprise Co. Ltd).

$$\text{Formal Quantum Efficiency(FQE)} = \frac{\text{rate of reaction}}{\text{total light intensity}} \times 100 \quad (4)$$

3. Results

3.1. Catalyst characterisation

The catalyst g-C_3N_4 is an organic polymer and is characterised by a layered graphitic-like structure. Its polyconjugated nature

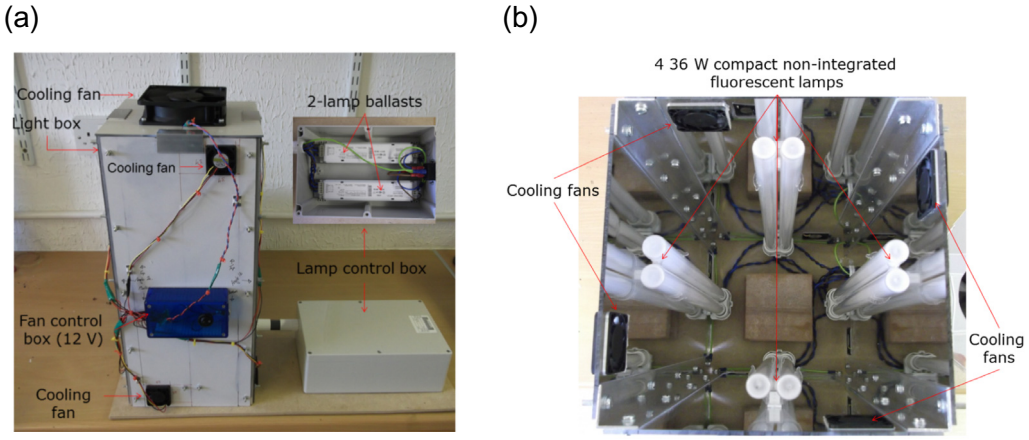

Fig. 3. (a) Image of light box with fan and lamp control boxes present and (b) image of light box from the top showing array of lights.

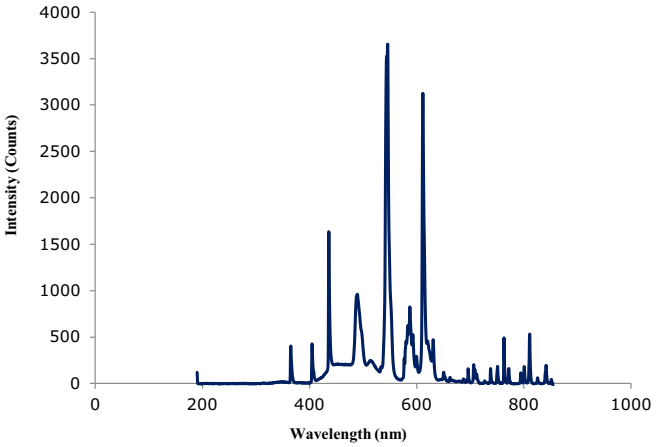

Fig. 4. Spectral output of the UV–Visible lamps.

makes it able to conduct electrons; however the orbital structure of carbon and nitrogen atoms makes it a semiconductor more than a conductive material, as is the case for graphite. This property, however, allows it to be a suitable candidate for photocatalytic processes, in particular water splitting.

The layered structure of g-C_3N_4 is reflected in the XRD pattern (Fig. 6) where the peak at $2\theta = 27.5°$ corresponds to an inter-layer d-spacing of 0.323 nm. This is similar to graphite inter-layer where the d-spacing is 0.326 nm. The small peak at $2\theta = 13.0°$ corresponds to an intra-layered-spacing of 0.681 nm.

For a photocatalyst to be able to perform water splitting, ideally the compound must have a band gap narrow enough for visible light absorption ($E_g < 3.0$ eV) but also wide enough to carry out the reaction ($E_g > 1.23$ eV). Graphitic carbon nitride fulfils these requirements. The UV–Vis spectrum (Fig. 7) of the sample shows an absorbance borderline between UV and visible irradiation (<500 nm) which translates into a band gap of 2.7 eV corresponding to the value reported in literature [21,22].

Fig. 8(a) shows a SEM image of the rough surface of g-C_3N_4 which results in a surface area of 13 $m^2\ g^{-1}$. Particle size was estimated at being, on average, 33 μm; however, bigger agglomerates were present. Layers of g-C_3N_4 are evident in the TEM image in Fig. 8(b).

The X-ray diffraction pattern (XRD) of the synthesized $NaTaO_3$ doped with La (2%) was confirmed to be perovskite-type crystalline structure as evident from the 2θ peaks that corresponded to the standard peak of $NaTaO_3$ (Fig. 9). The UV–Vis absorption spectrum of the Lanthanum doped $NaTaO_3$ was shown in Fig. 10(a), and the band gap of $NaTaO_3$·La was presented in Tauc plot calculated from its diffuse reflectance spectrum in Fig. 10(b). The absorption spectrum showed to be extended with Lanthanum doping as observed by the shoulder absorption around 340 nm. It indicated that it created a new energy level by a doped La at the upper level of the VB of non-doped $NaTaO_3$. The optical band gap was calculated as 3.0 eV (Fig. 10(b)), while the non-doped material was around 3.98 eV. Doping with La was found to be effective for both the utilisation of the light along with the charge separation of photogenerated electrons and holes compare to non-doped material.

3.2. Reactor performance

3.2.1. H_2 production

The photocatalytic production of H_2 over Pt-C_3N_4, g-C_3N_4 and $NaTaO_3$·La was monitored in the PFPR in order to evaluate the performance of the reactor. Reactor properties such as enhanced mass transport and illumination penetration and distribution were investigated in relation to photocatalytic activity. The results, shown in Tables 1 and 2, are displayed as 'total H_2 production' and 'photocatalytic H_2 production', which was required due to unexpected H_2 production observed in the control experiments.

The control experiments performed in this study showed that non-photocatalytic H_2 was evolving in the absence of a catalyst. This was concluded to be a result of the reaction between the sacrificial electron donor, oxalic acid, and SS propeller. The result of the corrosion was the formation of Fe^{2+} ions on the propeller surface and subsequently the generation of H_2 (Eqs. (5) and (6)).

$$Fe \rightarrow Fe^{2+} + 2e^- \quad (5)$$

$$2H^+ + 2e^- \rightarrow H_2 \quad (6)$$

The propeller was constructed from SS 316, which has an austenite structure with increased levels of Cr and Mo, which should prevent corrosion. It was observed, however, that there was a significant evolution of gas under control conditions; 58.1 μmol. It has been suggested that the extent to which corrosion is promoted is dependent upon the content of carbon in the steel and concentration of Fe^{2+} [41].

Typically under atmospheric conditions the corrosion of SS does not occur. Under more aggressive conditions such as acidic environments (pH < 1) the corrosion of SS has been reported [42–44]. While corrosion resistance under acidic conditions has been shown elsewhere in the literature [45], the results in this investigation

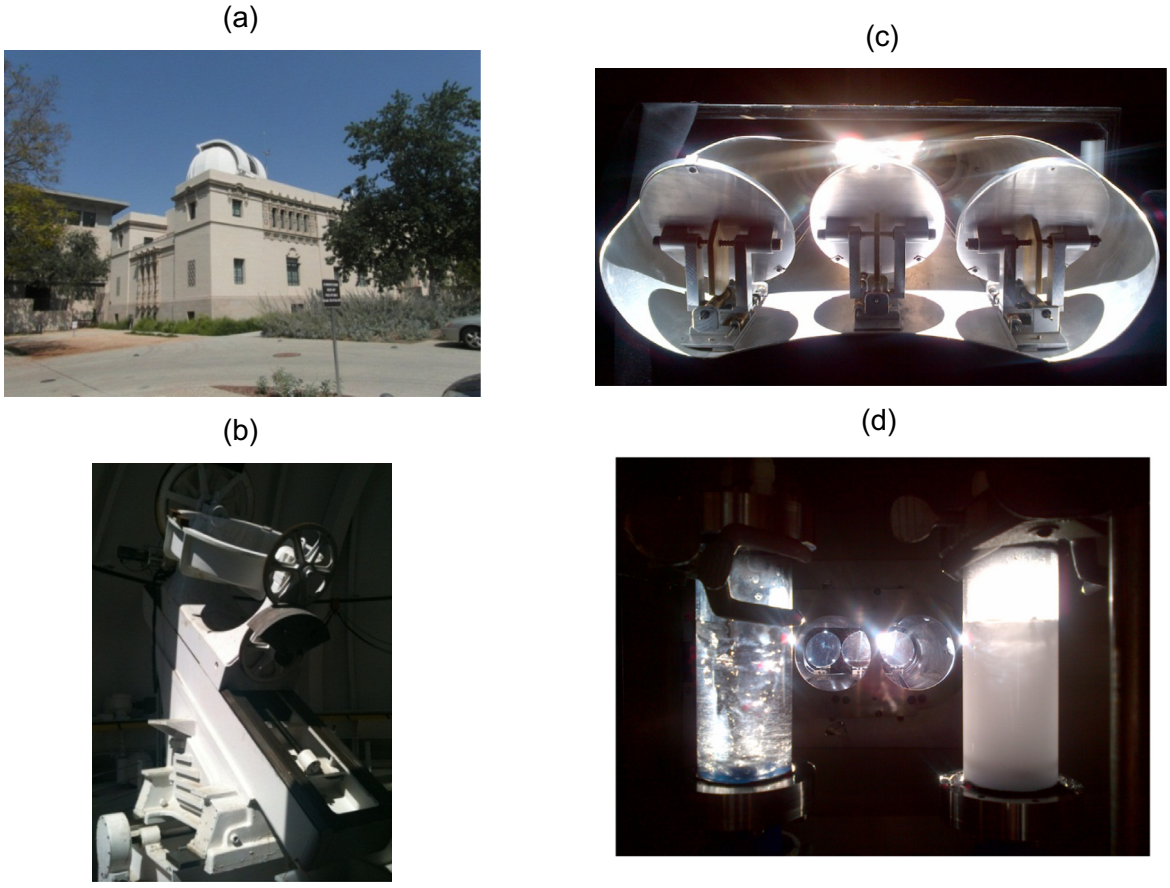

Fig. 5. The George Ellery Hale solar telescope. (a) The location of the telescope on the roof the Linda and Robinson building, (b) the mirrors which track the sun and guide light through the illumination shaft, (c) a series of subsequent light guiding mirrors and (d) two PFPR units under illumination from the telescope.

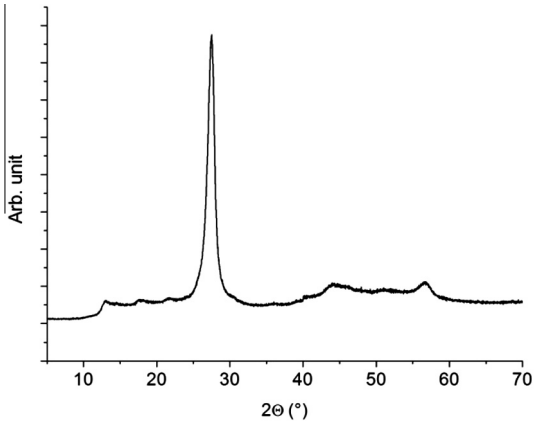

Fig. 6. XRD pattern of g-C_3N_4.

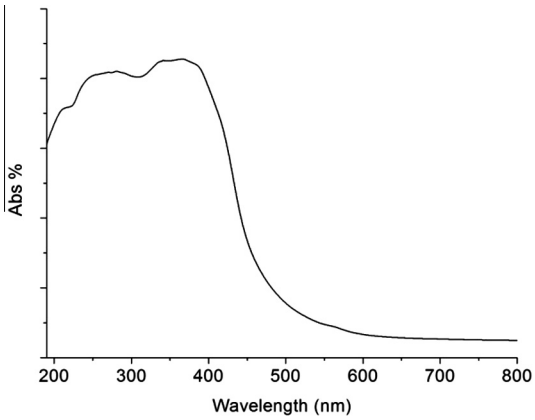

Fig. 7. UV–Vis absorption spectra of g-C_3N_4.

indicated that corrosion of the propeller had occurred resulting in 58.1 μmol H_2 production.

The results obtained from the control experiments showed that the level of H_2 produced was proportional to the level of corrosion. As the level of corrosion increased, the level of H_2 increased until a point at which the formation of Fe^{2+} products generated a temporary protective barrier which prevented further H_2 production. This protective barrier was eventually broken down as a result of prolonged contact with oxalic acid and corrosion continued generating H_2 [46]. Therefore, it was essential to investigate methods to prevent the continued corrosion of the propeller.

A number of conditions were investigated to minimise uncontrolled H_2 production including applying a thin polytetrafluoroethylene (PTFE) lining to the propeller surface to act as a barrier (Table 1). Table 1 shows the level of H_2 produced in the presence of Pt-C_3N_4 as a point of comparison for the control conditions. The results showed with no PTFE lining present H_2 evolution reached 58.1 μmol after 2 h illumination which is significantly higher than the 33.1 μmol H_2 produced in the presence of Pt-C_3N_4. The lower level of H_2 produced when Pt-C_3N_4 was present is likely due to the 'turbidity effect' which can occur when a catalyst is dispersed in a liquid medium. The agitation of the catalyst restricted the

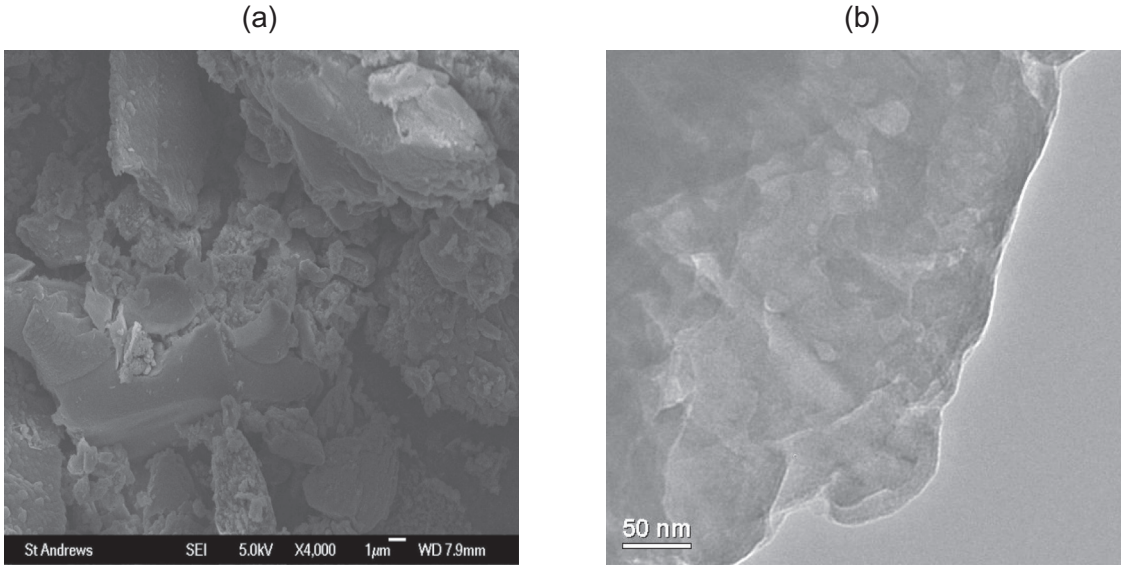

Fig. 8. (a) SEM and (b) TEM images of g-C_3N_4.

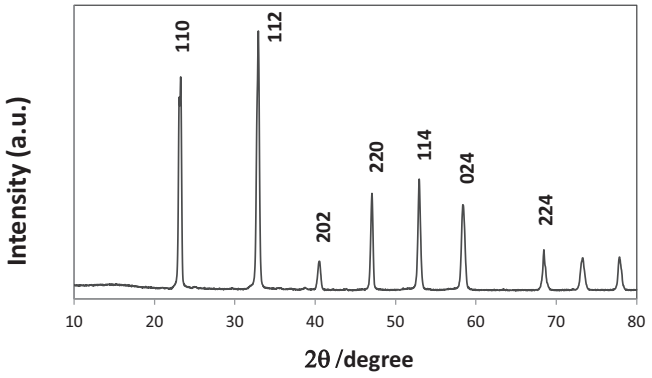

Fig. 9. X-ray diffraction pattern (XRD) of the synthesized $NaTaO_3$ doped with La (2%) powder shows to be perovskite-type crystal structure.

penetration of light and reduced the number of photons which reached the SS propeller. Placing a single PTFE lining on the propeller significantly decreased the H_2 produced by 76.94% from 58.1 to 13.4 μmol. Increasing the lining to 2-fold further decreased the corrosion process, as indicated by the reduction of H_2 to 4.8 μmol. Further increasing of the PTFE lining had no further effect on reducing the production of H_2, however, this did restrict the rotation of the propeller.

To demonstrate it was the corrosion of SS resulting in H_2 evolution, experiments in the absence of light, catalyst and oxalic acid were conducted. It is shown in Table 1 that no H_2 evolution was recorded in the absence of oxalic acid and a catalyst, however, H_2 was produced when there was oxalic present with and without illumination; 1.5 μmol H_2 under dark conditions. The level of H_2 produced in the absence of a catalyst, with and without light also showed the reaction was accelerated by the presence of photons. This aspect of the study highlights the need to conduct meticulous control experiments to ensure accurate results are obtained. In view of this fact, the production of H_2 from the corrosion of SS was monitored simultaneously in a second PFPR unit to ensure the photocatalytic activity could be accurately measured. The remaining results shown in this study as photocatalytic production were normalised to account for H_2 from corrosion.

The production of H_2 over the catalysts g-C_3N_4, Pt-C_3N_4 and $NaTaO_3$·La was monitored and is shown in Table 2. Positive photocatalytic H_2 values are shown for all catalysts indicating that there was H_2 evolution beyond that of the control values. Pt-C_3N_4 was shown to produce the largest volume of photocatalytic H_2 at 53.4 μmol with an evolution rate of 89 μmol h^{-1} g^{-1}. Over g-C_3N_4 and $NaTaO_3$·La the evolution of H_2 was significantly lower at 5

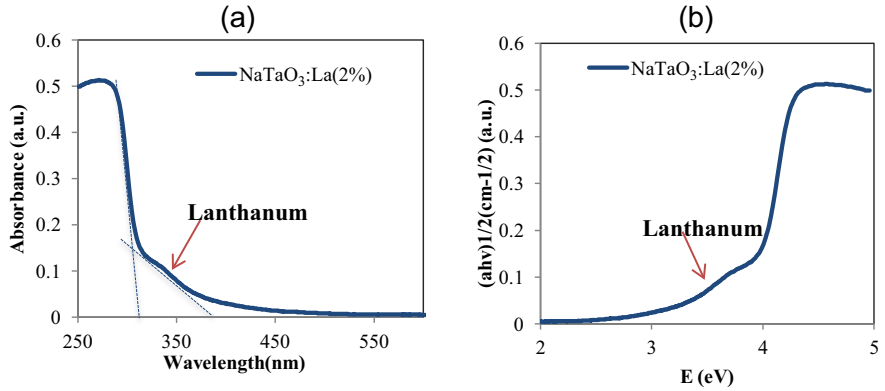

Fig. 10. (a) UV–Vis diffuse reflection spectrum of the $NaTaO_3$ doped with Lanthanum (2%); (b) Tauc plot of $NaTaO_3$:La.

Table 1
Production of H_2 over a range of experimental conditions. Irradiation provided by 144 W UV–Visible lamp for 120 min. The total light intensity was 396 μE cm^{-2} h^{-1}.

Illumination	Experiment condition	Reaction medium	H_2 (μmol)
144 W UV–Visible	No PTFE lining + Pt-C_3N_4	0.025 M oxalic acid	33.1
	No PTFE lining + no catalyst	0.025 M oxalic acid	58.1
	No PTFE lining + no catalyst	Distilled H_2O	0
	Single PTFE lining + no catalyst	0.025 M oxalic acid	13.4
	2-fold PTFE lining + no catalyst	0.025 M oxalic acid	4.8
Dark	No PTFE lining + no catalyst	0.025 M oxalic acid	1.5

and 8.3 μmol respectively. The photocatalytic activities were in the order Pt-C_3N_4 > $NaTaO_3$·La > C_3N_4.

An additional factor to be considered in the comparison of the photocatalysts is the absorption band edges of the catalysts in relation to the spectral output of the UV–Visible solar lamps (Fig. 4). While both catalysts were active under visible light, Pt-C_3N_4 (2.7 eV) showed stronger absorption than $NaTaO_3$·La (3.0 eV) in the range of 400–600 nm with $NaTaO_3$·La showing minimal absorbance beyond 450 nm.

H_2 production over C_3N_4 was 73.7% and 16.0% lower than Pt-C_3N_4 and $NaTaO_3$·La respectively. The enhanced activity of Pt-C_3N_4 was a result of Pt restricting the recombination of electrons and holes and catalysing proton reduction which has been well documented in the literature [26,38,47,48]. Pt has improved electron acceptor properties as a result of a larger work function (5.65 eV) as described by Mizukoshi et al. [48] which prevents the recombination of photo generated electrons and holes.

In any SED based H_2 producing system, it is also important to consider the role and pathway of the compound donating electrons. Oxalic acid was selected as the SED based on previous experiments conducted at the University of St. Andrews. As with any photocatalytic system that deploys a SED, the rate of production is limited by the depletion of the SED. Oxalic acid itself will undergo photocatalytic oxidation, ultimately resulting in complete mineralisation to CO_2 and H_2O. The depletion of oxalic acid was evident in the results obtained as the production profiles show the rate of H_2 production decreasing with prolonged irradiation. The photodecomposition via oxidation by holes in the valence band favours molecules that are easily absorbed onto the surface (Eq. (7)).

$$h^+_{vb} + C_2H_2O_{4(ads^{\cdot})} = C_2H_2O_{4(ads^{\cdot+})} \quad (7)$$

Alternatively, however, decomposition can occur via interaction with OH· on the catalyst surface and in bulk (Eq. (8)).

$$OH_{ads/bulk^{\cdot}} + C_2H_2O_{4_{ads/bulk}} = C_2H_2O_{4(ads^{\cdot+})} \quad (8)$$

As the reactor was a sealed unit, which was purged prior to operation, the role of O_2^{-} in oxalic acid decomposition was thought to be minimal. The overall mineralisation of oxalic acid is shown in Eq. (9). The final products are CO_2 and H_2O, with few intermediates being reported in the literature.

$$2H_2C_2O_4 + O_2 + 2h\nu = 4CO_2 + 2H_2O \quad (9)$$

3.2.2. Effect of mass transfer

While the importance of mass transfer is well understood in photocatalytic processes along with the elimination of such effects, there are few examples in the literature which investigate the impact of varying the level of mass transfer to achieve optimisation. Furthermore, there are currently no examples of a propeller based fluidised system deployed as photocatalytic reactors for hydrogen generation from water. It has been found that increasing the speed at which the propeller rotated had a number of effects; reduced mass transfer, increased light penetration and conversion of laminar flow to turbulent. The primary physical response of increasing the propeller speed was the cavitation of the aqueous medium over the range of 0–1730 rpm (Fig. 11).

The effect of propeller speed on H_2 production over Pt-C_3N_4 using rotational speeds of 0–1730 rpm is shown in Fig. 12. The results show at a range of 0–1035 rpm, the evolution of H_2 was directly proportional to the speed of the propeller. The total production of H_2 steadily increased from 15.9 to 42.4, 55.2 and 65.7 μmol at 0, 289, 692 and 1035 rpm respectively. Thereafter, however, an increase in propeller speed to 1384 rpm showed no further increase in H_2, with a concentration of 65.2 μmol at 1384 rpm. Moreover, once the propeller reached the maximum speed of 1730 rpm the production of H_2 reduced to 61.9 μmol. In the PFPR, the cavitation of the reaction medium began at 289 rpm which was indicated by the significant increase of 62.5% H_2 production from 0 to 289 rpm. It was also seen that as cavitation increased towards its maximum point at 1035 rpm, the rate of production increased; 23.73% and 15.98% H_2 production increase from 289 to 692 rpm and 692 to 1035 rpm respectively. As the cavitation generated at 1035 rpm was not exceeded at greater speeds, the evolution of H_2 was seen to begin to decrease: a 0.76% reduction of H_2 from 1035 to 1384 rpm and 5.06% from 1384 to 1730 rpm.

The effect of propeller speed on H_2 production can be considered with a view towards mass transfer and light penetration. At 0 rpm, the system was evidentially mass transport limited, with the reaction rate dictated by the settling velocity of the catalyst, which ultimately formed a dense bed at the base of the reactor. The significant increase in production at 289 rpm (62.5%) demonstrated the impact of reducing mass transfer limitations and increasing light penetration. At the initial point of cavitation, the dense catalyst bed is brought to a point of fluidisation as the propeller creates uniformed movement of both reactant and catalyst, generating multiple interactions on the surface of the catalyst. This relationship is further enhanced by increasing the speed of the propeller to 1035 rpm, as indicated by the H_2 production rate. Within this range, the propeller forced the aqueous reaction medium towards the wall of the unit creating full dispersion of the catalyst bed and reducing the depth of penetration required for photons to reach the catalyst surface. This feature also created maximum exposure of the aqueous medium to the 360° irradiation array.

An interesting aspect of this work was as the speed increased to 1384 and 1730 rpm, the results indicated that mass transfer limitations were no longer predominant. The plateau and further drop (5.06%) in H_2 production at 1384 and 1730 rpm highlight that the propeller speed was no longer directly proportional to production.

Table 2
Photocatalytic H_2 production shown as concentration and rate over Pt-C_3N_4, g-C_3N_4 and $NaTaO_3$:La. Conditions; 100 mL H_2O with oxalic acid (0.025 M) with 1 g L^{-1} catalyst loading. Irradiation provided by 144 W UV–Visible lamp for 360 min with samples taken at 2 h intervals. The total light intensity was 396 μE cm^{-2} h^{-1}.

Catalyst	Total H_2 evolution (μmol)	Photocatalytic H_2 evolution	Photocatalytic H_2 evolution rate (μmol h^{-1} g^{-1})	Formal Quantum Efficiency (%)
Pt-C_3N_4	65.7	53.4	89	2.25
C_3N_4	17.3	2.5	4	0.11
$NaTaO_3$·La	20.6	4.1	7	0.17

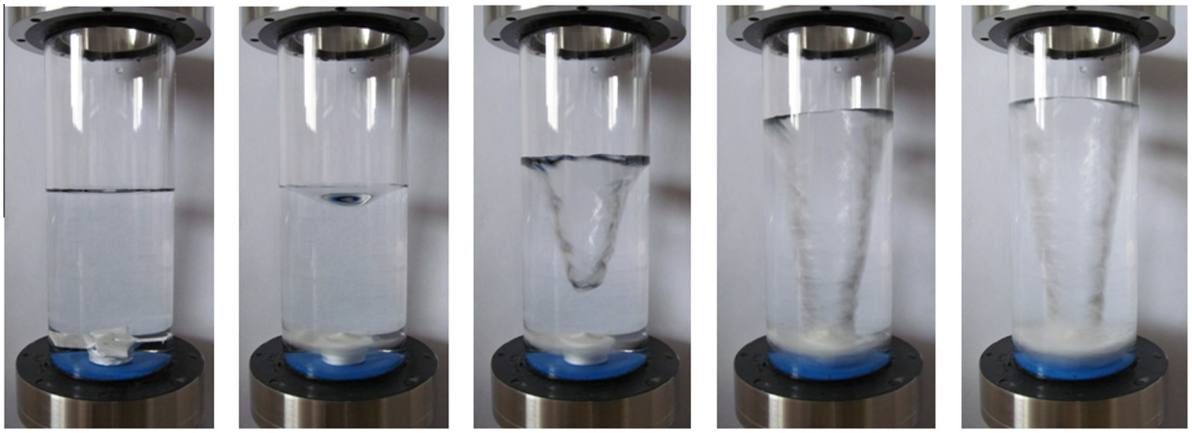

Fig. 11. The formation of cavitation over a range of 0–8 dcV.

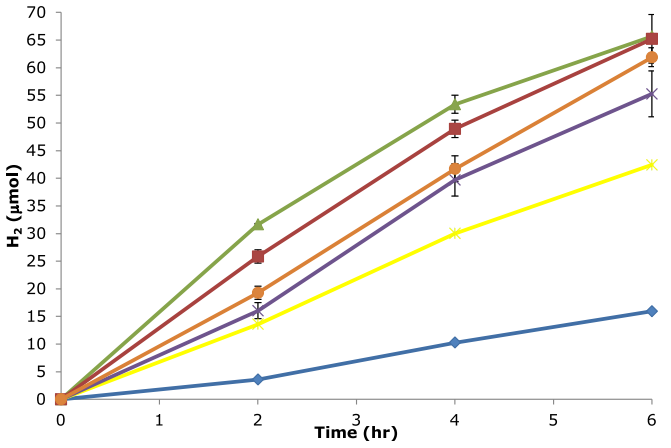

Fig. 12. Effect of rotational speed on H_2 production over Pt-C_3N_4 under UV–Visible irradiation at 0 rpm (blue line), 346 rpm (yellow line), 692 rpm (purple line), 1035 rpm (green line), 1384 rpm (red line) and 1730 rpm (orange line). Conditions; 100 mL H_2O with oxalic acid (0.025 M) with 1 g L^{-1} catalyst loading. Irradiation was provided by 144 W UV–Visible lamp for 360 min with samples taken at 2 h intervals. The total light intensity was 396 µE cm^{-2} h^{-1}. (For interpretation of the references to color in this figure legend, the reader is referred to the web version of this article.)

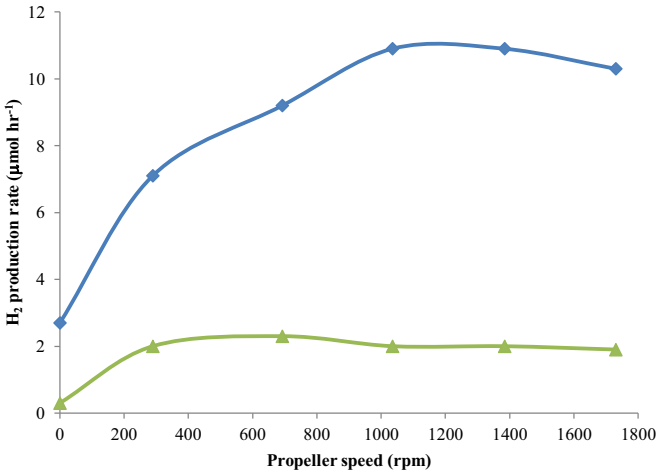

Fig. 13. Relationship between H_2 production and propeller rotational speed in the presence (red line) and absence (blue line) of Pt-C_3N_4. Conditions; 100 mL H_2O with oxalic acid (0.025 M) with 1 g L^{-1} catalyst loading. The propeller was operated in the range of 0–1730 rpm. Irradiation provided by 144 W UV–Visible lamp for 360 min with samples taken at 2 h intervals. The total light intensity was 396 µE cm^{-2} h^{-1}. (For interpretation of the references to color in this figure legend, the reader is referred to the web version of this article.)

At 1035 rpm, the aqueous medium had already reached its maximum height and thus increasing the speed of the propeller further would have no impact. Therefore, the depth of penetration required for photon adsorption at 1035 rpm was equal to that at 1384 and 1730 rpm. The level of interaction at 1384 and 1730 rpm, however, was possibly altered as a result of increased speed. The agglomeration of Pt-C_3N_4 to form 'catalyst clusters', along with the trapping of the catalyst around the propeller may have prevented the material from being fully fluidised. As a result, mass transport limitations are increased as the available catalyst surface for photocatalytic reactions to take place was reduced. The overall result was the observed drop in H_2 production rate at increased propeller speeds.

Fig. 13 shows the evolution rate of H_2 with and without Pt-C_3N_4 over a range of rotational speeds. The highest rate of total H_2 production was 109 µmol h^{-1} g^{-1} at 1035 rpm. As it is not appropriate to display H_2 production from corrosion as per gram of catalyst, all rates shown in this figure are displayed as rate per h of irradiation. As is shown in Fig. 13 the propeller rotational speed also impacted the release of non-photocatalytic H_2 from the propeller. At increased speeds (1035 and 1384 rpm) and maximum cavitation the corrosion of SS and thus the production of H_2 was observed to decrease and plateau, 2.0 and 1.9 µmol h^{-1} H_2 at 1384 and 1730 rpm respectively. This was a result of a reduced contact time between the blade surface of the propeller and oxalic acid. At lower speeds (⩽692 rpm), however, full cavitation of the liquid medium had not occurred, which increased the residual time between oxalic acid and SS, subjecting the propeller to corrosion and thus H_2 production to occur, Fig. 13 also indicates the optimum rotational speed of the propeller to be 1035 rpm based upon levels of H_2 produced under the experimental conditions. At 1035 rpm the greatest difference in H_2 production when Pt-C_3N_4 was present and absent was recorded at 8.94 µmol h^{-1}. The remaining propeller speeds were in the order 1384 rpm (8.86 µmol h^{-1}) > 1035 rpm (8.4 µmol h^{-1}) > 692 rpm (6.93 µmol h^{-1}) > 289 rpm (5.14 µmol h^{-1}) > 0 rpm (2.48 µmol h^{-1}).

In order to determine the overall efficiency of the photocatalytic system, Table 3 shows the formal quantum efficiency (FQE) of H_2 produced in the PFPR over the range of 0–1730 rpm. As indicated by the reaction rate, the highest FQE of 2.25% was achieved when the propeller rotational speed was set to 1035 rpm. This calculation was a more appropriate means of displaying photocatalytic efficiency in this study as it takes into account the total light intensity of a broad spectrum source, as oppose to the photonic

Table 3
The calculated FQE for the production of H_2 in the PFPR over the propeller rotational speed range of 0–1730 rpm. The FQE was determined using Eq. (4) and a total light intensity of 396 μE cm^{-2} h^{-1}.

Propeller speed (rpm)	Formal Quantum Efficiency (%)
0	0.61
289	1.29
692	1.74
1035	2.25
1384	2.24
1730	2.12

efficiency calculation which is based on a monochromatic wavelength. This has previously been reported and discussed by Eggins et al. and Mills and LeHunte [40,49].

Comparison of the overall performance of the PFPR to units previously reported in the literature is difficult. Generally, the comparison of different photocatalytic systems is challenging as there are a number of varying parameters which must be taken into consideration including; catalyst properties, intensity of the illumination source, reactor geometry, pH and method of mass transfer [40]. The comparison of quantum yield and photonic efficiencies provides an indication of the overall efficiency and in occasional circumstances a platform to evaluate different photocatalytic systems. In relation to the work presented here, however, comparison of the novel PFPR to other reported reactors is challenging as the calculated FQE is not directly comparable to photonic efficiencies and apparent quantum yields reported when using a monochromatic light source. Moreover, there are currently few examples of reactors deployed for H_2O reduction to which a comparison could be made. It is, however possible to draw some comparisons with the study conducted by Reilly and colleagues in 2012. Similarities exist between their unit and the PFPR as both adopted an annular geometric design with low power illumination, along with a simple design concept to ensure the unit was not overly complex. Reilly et al. adopted a centrally positioned internal illumination source along with a more traditional style of fluidisation through the recirculation of the liquid media, which resulted in agitation of the catalyst bed. As no photonic efficiencies were reported in this paper, cross-comparison must be based on reaction yields and rates. The Reilly et al. fluidised system produced an optimum H_2 rate of 198 μmol h^{-1} which was significantly higher than the hourly rate of H_2 produced in the PFPR (~8.9 μmol h^{-1}). To accurately compare these systems however, the following reaction conditions must be considered; catalyst loading, illumination time frame and source. The fluidised system described by Reilly et al. used a high catalyst loading weight of 80 g, along with UV light and 24 h irradiation. Interestingly, if the rate of H_2 production was to be displayed as μmol g^{-1} h^{-1}, as it often is, the rate would be ~2.475 μmol g^{-1} h^{-1}, which was significantly lower than that of 89 μmol g^{-1} h^{-1} produced in the PFPR. Furthermore, the catalysts deployed in PFPR were novel synthesised for excitation under UV–Vis and natural illumination, while the Pt-loaded TiO_2 catalyst developed by Reilly et al. was restricted to UV light.

3.3. Preliminary solar H_2 production over $NaTaO_3$·La

If photocatalytic production of H_2 is to be utilised as an alternative fuel it is essential that the development of photocatalytic reactors focuses towards systems which are capable of converting solar energy. Solar driven photocatalysis has been reported in the literature primarily for the applications of water detoxification [50,51], CO_2 reduction [52,53] and H_2 production [31,32,35]. To date, however, there are no examples of solar H_2 production from the use of a solar telescope to concentrate the stream of photons. Jing et al. [7] discussed a number of parameters which restrict the application of solar driven photocatalysis including the inability to efficiently utilise natural light. One such limitation of solar driven photocatalysis is the requirement to first concentrate the stream of photons, which can result in a change in temperature and subsequently a change in pressure. In using the solar telescope these limitations are eliminated which prevents a thermal reaction taking place over that of a photocatalytic one.

Solar H_2 production over $NaTaO_3$·La (which was the available catalyst at the time of testing) in the PFPR is shown in Table 4. Under entirely natural solar light a total concentration of 4.6 μmol H_2 was generated which gave a total production rate of 8 μmol h^{-1} g^{-1}. The evolution of H_2 from the corrosion of the propeller was also monitored simultaneously in a second PFPR unit and was found to be lower at 1.7 μmol, 63.0% lower than when $NaTaO_3$·La was present. Therefore, a calculated photocatalytic H_2 evolution rate of 5 μmol h^{-1} g^{-1} was achieved under concentrated solar illumination.

The total production of H_2 over $NaTaO_3$·La and the photocatalytic production of H_2 under UV–Visible and natural solar light are also summarised in Table 3. While H_2 production is lower under solar light, the results remain promising. In order for photocatalysis to progress there is a need for both solar activated materials and reactors that can maximise their efficiency. The PFPR quartz body provided a large surface area for solar irradiation whilst the propeller increased mass transfer to increase the activity of the catalyst.

While the production of H_2 under solar illumination was lower than under artificial light, there are factors which must be considered; the electromagnetic spectrum of natural and artificial light, the photon delivery system of the solar irradiation source and variable nature of solar irradiation itself. The solar telescope used in this preliminary investigation continually monitored and tracked sun light during the day and concentrated it through a series of gold plated mirrors and illumination shafts. This allowed for a concentrated stream of solar photons to be guided to the tubular body of the PFPR. It has been reported by Jing et al. 2009 [32] that the concentration of solar light is essential, stating that 'a solar reactor cannot be designed without first concentrating natural sunlight in an attempt to enhance the intensity'. As the electromagnetic spectrum of solar light has a broad spectrum in comparison to the narrow range emitted from high power lamps, which are typically adopted in photocatalytic systems, the intensification of the illumination source is essential. The concentration of natural light in this circumstance was achieved while maintaining atmospheric conditions and room temperature which ensured the production of hydrogen was photocatalytic and not thermally activated.

While the mirrors and shafts of the solar telescope concentrated the irradiation stream, the light path was subject to contaminants. Bickley et al. [54] stated that the number of particles and contaminants between the source of exposure and the catalyst should be kept to a minimum. Under UV–Visible light, the source of illumination is typically immersed or externally positioned in close

Table 4
Total and photocatalytic H_2 evolution and rate over $NaTaO_3$·La under UV–Visible and natural solar illumination. Conditions; 100 mL H_2O with oxalic acid (0.025 M) with 1 g L^{-1} catalyst loading. UV–Visible irradiation provided by 144 W lamps. The irradiation time for both artificial and natural illumination was 360 min with samples taken at 2 h. intervals.

Illumination	Total H_2 evolution (μmol)	Photocatalytic H_2 evolution (μmol)	Photocatalytic H_2 evolution rate (μmol g^{-1} h^{-1})
144 W UV–Visible	20.6	8.3	14
Solar telescope	4.6	2.9	5

proximity to the reactor and as such prevents the presence of contaminants in the light path. In comparison the light path of the George Ellery Hale telescope is approximately 40 ft, and is exposed to various environmental contaminants.

The weather dependency and variable nature of solar light as an irradiation source is also a key factor. Cloud coverage and unexpected weather can reduce and restrict the delivery of light through the telescope. The result of which can be dark periods which reduces the photocatalytic efficiency.

4. Conclusions

In summary, the production of H_2 over Pt-C_3N_4 and $NaTaO_3$·La under UV–Visible light and natural solar irradiation was achieved in a novel fluidised photo reactor. The reactor properties were also shown to enhance the photocatalytic activity of the system with an increase from 24 μmol h^{-1} g^{-1} at 0 rpm to 89 μmol h^{-1} g^{-1} at 1035 rpm. At increased speeds of 1384 and 1730 the rate of H_2 produced decrease indicating mass transport limitations no longer predominant at speeds greater than 1035 rpm. A limitation to the current design of the PFPR is the uncontrolled production of H_2 as a result of SS corrosion by oxalic acid. The corrosion was localised to the propeller and was reduced by operating the propeller at 1035 rpm and applying a PTFE coating to the surface. The evolution of H_2 over $NaTaO_3$·La under solar illumination was also achieved with a production rate of 5 μmol h^{-1} g^{-1}. These initial results demonstrate the potential for solar water reduction for H_2 production from a sustainable source. This is a key area of focus for current ongoing work being conducted.

Acknowledgments

This work was funded under the joint UK/US EPSRC/NSF International Collaboration in Chemistry Programme, Project number EP/H004130/1. The authors would like to thank the funders for their support which enabled this research to be carried out.

References

[1] S. Das, W.M.A. Wan, Daud, Photocatalytic CO_2 transformation into fuel: a review on advances in photocatalyst and photoreactor, Renew. Sustain. Energy Rev. 39 (2014) 765–805.
[2] T. Inoue, A. Fujishima, S. Konishi, K. Honda, Photoelectrocatalytic reduction of carbon dioxide in aqueous suspensions of semiconductor powders, Nature 277 (1979) (1979) 637–638.
[3] M. Anpo, Photocatalytic reduction of CO_2 with H_2O on highly dispersed Ti-oxide catalysts as a model of artificial photosynthesis, J. CO_2 Utilization 1 (2013) 8–17.
[4] K. Li, X. An, K. Park, M. Khraisheh, J. Tang, A critical review of CO_2 photoconversion: catalysts and reactors, Catal. Today 224 (2014) 3–12.
[5] K. Maeda, Photocatalytic water splitting using semiconductor particles: history and recent developments, J. Photochem. Photobiol., C 12 (2011) 237–268.
[6] A. Midilli, I. Dincer, Hydrogen as a renewable and sustainable solution in reducing global fossil fuel consumption, Int. J. Hydrogen Energy 33 (2008) 4209–4222.
[7] D. Jing, L. Guo, L. Zhao, X. Zhang, H. Liu, M. Li, S. Shen, G. Liu, X. Hu, X. Zhang, K. Zhang, L. Ma, P. Guo, Efficient solar hydrogen production by photocatalytic water splitting: from fundamental study to pilot demonstration, Int. J. Hydrogen Energy 35 (2010) 7087–7097.
[8] R. Molinari, T. Marino, P. Argurio, Photocatalytic membrane reactors for hydrogen production from water, Int. J. Hydrogen Energy 39 (2014) 7247–7261.
[9] Y. Sasaki, H. Kato, A. Kudo, $[Co(bpy)_3]^{3+/2+}$ and $[Co(phen)_3]^{3+/2+}$ electron mediators for overall water splitting under sunlight irradiation using Z-scheme photocatalyst system, J. Am. Chem. Soc. 135 (2013) 5441–5449.
[10] M. Kitano, K. Tsujimaru, M. Anpo, Decomposition of water in the separate evolution of hydrogen and oxygen using visible light-responsive TiO_2 thin film photocatalysts: effect of the work function of the substrates on the yield of the reaction, Appl. Catal. A 314 (2006) 179–183.
[11] E. Selli, G.L. Chiarello, E. Quartarone, P. Mustarelli, I. Rossetti, L. Forni, A photocatalytic water splitting device for separate hydrogen and oxygen evolution, Chem. Commun. (2007) 5022–5024.
[12] S. Yu, C. Huang, C. Liao, J.C.S. Wu, S. Chang, K. Chen, A novel membrane reactor for separating hydrogen and oxygen in photocatalytic water splitting, J. Membr. Sci. 382 (2011) 291–299.
[13] K. Fujihara, T. Ohno, M. Matsumura, Splitting of water by electrochemical combination of two photocatalytic reactions on TiO_2 particles, J. Chem. Soc. – Faraday Trans. 94 (1998) 3705–3709.
[14] C. Lo, C. Huang, C. Liao, J.C.S. Wu, Novel twin reactor for separate evolution of hydrogen and oxygen in photocatalytic water splitting, Int. J. Hydrogen Energy 35 (2010) 1523–1529.
[15] N. Skillen, C. McCullagh, M. Adams, Photocatalytic Splitting of Water, Springer, Berlin Heidelberg, 2014. pp. 1–42.
[16] K. Reilly, F. Taghipour, D.P. Wilkinson, Photocatalytic hydrogen production in a UV-irradiated fluidized bed reactor, Energy Procedia 29 (2012) 513–521.
[17] H.P. Kuo, C.T. Wu, R.C. Hsu, Continuous toluene vapour photocatalytic deduction in a multi-stage fluidised bed, Powder Technol. 210 (2011) 225–229.
[18] S. Matsuda, H. Hatano, Photocatalytic removal of NO_x in a circulating fluidized bed system, Powder Technol. 151 (2005) 61–67.
[19] R. Zhu, S. Che, X. Liu, S. Lin, G. Xu, F. Ouyang, A novel fluidized-bed-optical-fibers photocatalytic reactor (FBOFPR) and its performance, Appl. Catal. A 471 (2014) 136–141.
[20] C. Si, J. Zhou, H. Gao, G. Liu, Photocatalytic degradation of formaldehyde in a fluidized bed with sound-magnetic assistance, Adv. Powder Technol. 24 (2013) 295–300.
[21] R.L. Pozzo, R.J. Brandi, A.E. Cassano, M.A. Baltanás, Photocatalytic oxidation of oxalic acid in dilute aqueous solution, in a fully illuminated fluidized bed reactor, Chem. Eng. Sci. 65 (2010) 1345–1353.
[22] H. Liu, Q. Guo, Fluidization in combined acoustic-magnetic field for mixtures of ultrafine particles, China Particuol. 5 (2007) 111–115.
[23] P. Zeng, T. Zhou, J. Yang, Behavior of mixtures of nano-particles in magnetically assisted fluidized bed, Chem. Eng. Process. 47 (2008) 101–108.
[24] S. Liu, H. Syu, One-step fabrication of N-doped mesoporous TiO_2 nanoparticles by self-assembly for photocatalytic water splitting under visible light, Appl. Energy 100 (2012) 148–154.
[25] T. Sreethawong, S. Yoshikawa, Enhanced photocatalytic hydrogen evolution over Pt supported on mesoporous prepared by single-step sol–gel process with surfactant template, Int. J. Hydrogen Energy 31 (2006) 786–796.
[26] J. Yang, H. Yan, X. Wang, F. Wen, Z. Wang, D. Fan, J. Shi, C. Li, Roles of cocatalysts in Pt–PdS/CdS with exceptionally high quantum efficiency for photocatalytic hydrogen production, J. Catal. 290 (2012) 151–157.
[27] Z. Khan, M. Qureshi, Tantalum doped $BaZrO_3$ for efficient photocatalytic hydrogen generation by water splitting, Catal. Commun. 28 (2012) 82–85.
[28] H. Jeong, T. Kim, D. Kim, K. Kim, Hydrogen production by the photocatalytic overall water splitting on: effect of preparation method, Int. J. Hydrogen Energy 31 (2006) 1142–1146.
[29] S.C. Yan, Z.Q. Wang, Z.S. Li, Z.G. Zou, Photocatalytic activities for water splitting of La-doped-$NaTaO_3$ fabricated by microwave synthesis, Solid State Ionics 180 (2009) 1539–1542.
[30] W. Fan, Z. Zhou, W. Xu, Z. Shi, F. Ren, H. Ma, S. Huang, Preparation of $ZnIn_2S_4$/fluoropolymer fiber composites and its photocatalytic H_2 evolution from splitting of water using Xe lamp irradiation, Int. J. Hydrogen Energy 35 (2010) 6525–6530.
[31] C.A. Linkous, T.E. Mingo, N.Z. Muradov, Aspects of solar hydrogen production from hydrogen sulfide using semiconductor particulates, Int. J. Hydrogen Energy 19 (1994) 203–208.
[32] D. Jing, H. Liu, X. Zhang, L. Zhao, L. Guo, Photocatalytic hydrogen production under direct solar light in a CPC based solar reactor: Reactor design and preliminary results, Energy Convers. Manage. 50 (2009) 2919–2926.
[33] C. Liu, Z. Lei, Y. Yang, Z. Zhang, Preliminary trial on degradation of waste activated sludge and simultaneous hydrogen production in a newly-developed solar photocatalytic reactor with AgX/TiO_2-coated glass tubes, Water Res. 47 (2013) 4986–4992.
[34] K. Villa, X. Domènech, S. Malato, M.I. Maldonado, J. Peral, Heterogeneous photocatalytic hydrogen generation in a solar pilot plant, Int. J. Hydrogen Energy 38 (2013) 12718–12724.
[35] C.A. Linkous, N.Z. Muradov, S.N. Ramser, Consideration of reactor design for solar hydrogen production from hydrogen sulfide using semiconductor particulates, Int. J. Hydrogen Energy 20 (1995) 701–709.
[36] H. Kato, K. Asakura, A. Kudo, Highly efficient water splitting into H_2 and O_2 over lanthanum-doped $NaTaO_3$ photocatalysts with high crystallinity and surface nanostructure, J. Am. Chem. Soc. 125 (2003) 3082–3089.
[37] X. Xu, G. Liu, C. Randorn, J.T.S. Irvine, G-C_3N_4 coated $SrTiO_3$ as an efficient photocatalyst for H_2 production in aqueous solution under visible light irradiation, Int. J. Hydrogen Energy 36 (2011) 13501–13507.
[38] X. Wang, K. Maeda, A. Thomas, K. Takanabe, G. Xin, J.M. Carlsson, K. Domen, M. Antonietti, A metal-free polymeric photocatalyst for hydrogen production from water under visible light, Nat. Mater. 8 (2009) 76–80.
[39] Q. Wang, N. An, W. Chen, R. Wang, F. Wang, Z. Lei, W. Shangguan, Photocatalytic water splitting into hydrogen and research on synergistic of Bi/Sm with solid solution of Bi–Sm–V photocatalyst, Int. J. Hydrogen Energy 37 (2012) 12886–12892.
[40] B.R. Eggins, P.K.J. Robertson, E.P. Murphy, E. Woods, J.T.S. Irvine, Factors affecting the photoelectrochemical fixation of carbon dioxide with semiconductor colloids, J. Photochem. Photobiol. A. 118 (1998) 31–40.
[41] M.S. Abdel Aal, M.H. Wahdan, G.K. Gomma, Influence of Fe^{2+} ion on the corrosion of carbon steel, Mater. Chem. Phys. 39 (1995) 290–297.

[42] B.J. Wiersma, Corrosion Mechanisms and Rates for Carbon Steel and Stainless Steel Materials Exposed to Oxalic Acid Solutions, USA; U.S. Department of Energy (2004).
[43] B.J. Wiersma, Hydrogen Generation During the Corrosion of Carbon Steel in Oxalic Acid, The U.S. Department of Energy, USA, 2004.
[44] I. Sekine, C. Okano, Corrosion behavior of mild steel and ferritic stainless steels in oxalic acid solution, Corrosion 45 (1989) 924–932.
[45] A.H.C. Chan, C.K. Chan, J.P. Barford, J.F. Porter, Solar photocatalytic thin film cascade reactor for treatment of benzoic acid containing wastewater, Water Res. 37 (2003) 1125–1135.
[46] B.J. Wiersma, J.I. Mickalonis, D.C. Beam, M.R. Poirier, D.T. Herman, S.D. Fink, J. M. Pareizs, F.F. Fondeur, In-situ Monitoring of Corrosion during a Laboratory Simulation of Oxalic Acid Chemical Cleaning, U.S. Department of Energy, USA, 2004.
[47] X. Zheng, L. Wei, Z. Zhang, Q. Jiang, Y. Wei, B. Xie, M. Wei, Research on photocatalytic H_2 production from acetic acid solution by Pt/TiO_2 nanoparticles under UV irradiation, Int. J. Hydrogen Energy 34 (2009) 9033–9041.
[48] Y. Mizukoshi, Y. Makise, T. Shuto, J. Hu, A. Tominaga, S. Shironita, S. Tanabe, Immobilization of noble metal nanoparticles on the surface of TiO_2 by the sonochemical method: Photocatalytic production of hydrogen from an aqueous solution of ethanol, Ultrason. Sonochem. 14 (2007) 387–392.
[49] A. Mills, S. Le Hunte, An overview of semiconductor photocatalysis, J. Photochem. Photobiol. A 108 (1997) 1–35.
[50] V. Benz, M. Muller, D.W. Bahnemann, D. Weichgrebe, M. Brehm, Reaktoren für die photokatalytische abwasserreinigung mit stegmehrfachplatten als solarelemente, Deutsche Offenlegungsschrift (DE) 195 (1996) 372.
[51] R. Dillert, A.E. Cassano, R. Goslich, D. Bahnemann, Large scale studies in solar catalytic wastewater treatment, Catal. Today 54 (1999) 267–282.
[52] J.C.S. Wu, H. Lin, C. Lai, Photo reduction of CO_2 to methanol using optical-fiber photoreactor, Appl. Catal. A 296 (2005) 194–200.
[53] T. Wang, L. Yang, X. Du, Y. Yang, Numerical investigation on CO_2 photocatalytic reduction in optical fiber monolith reactor, Energy Convers. Manage. 65 (2013) 299–307.
[54] R.I. Bickley, M.J. Slater, W. Wang, Engineering development of a photocatalytic reactor for waste water treatment, Process Saf. Environ. Prot. 83 (2005) 205–216.